Title

Conductive Polymer Binder-Enabled Cycling of Pure Tin Nanoparticle Composite Anode Electrodes for a Lithium-Ion Battery

Journal

Journal of The Electrochemical Society, 160(6)

ISSN

0013-4651

Authors

Xun, Shidi
Song, Xiangyun
Battaglia, Vincent
et al.

Publication Date

2013

DOI

10.1149/2.087306jes

Peer reviewed

Conductive Polymer Binder-Enabled Cycling of Pure Sn Nanoparticle Composite Anode Electrodes for a Lithium-ion Battery

By

Shidi Xun, Xiangyun Song, Vincent Battaglia, and Gao Liu*

Lawrence Berkeley National Laboratory, 1 Cyclotron Rd., Berkeley, CA 94720, USA
* Corresponding author: gliu@lbl.gov

ABSTRACT

Pure tin (Sn) nanoparticles can be cycled in stable and high gravimetric capacity (> 500 mAh/g) with a polyfluorene-type conductive polymer binder in composite electrodes. Crystalline Sn nanoparticles (< 150 nanometers, nm) were used as anode materials in this study. The average diameter of Sn secondary particles is 270 nm, calculated based on BET surface area. The composite electrodes contain a conductive polymer binder that constitutes 2% to 10% of the material, without any conductive additives (e.g., acetylene black). The electrode containing the 5% conductive binder showed the best cycling performance, with a reversible capacity of 510 mAh/g. Crystallinity of Sn particles gradually degrades during cycling, and pulverization of particles was observed after long-term cycling, leading to the capacity fade. The conductive polymer binder shows advantages over other conventional binders, such as poly(vinylidene fluoride) (PVDF) and carboxymethylcellulose (CMC) binders, because it can provide electrical conductivity and strong adhesion during Sn volume expansion.

KEYWORDS: batteries, lithium-ion, conductive polymer, binder, tin

1. Introduction

Group III and IV metallic or metalloid materials (e.g., Si, Sn, Ge, Mg and Al) have attracted significant attention as potential anode materials for lithium-ion batteries due to their high capacity to alloy with lithium. However, the high capacity of the materials to alloy comes with a proportional volume change upon lithiation and delithiation with lithium during the electrochemical cycling. This volume change generates a structural breakdown of the electrode, leading to performance degradation. Metallic Sn is one of the most promising candidates to substitute for conventional graphite anode material for rechargeable batteries (such as those used in consumer electronics or electric vehicles) because of its high theoretical specific capacity—994 mAh/g ($Li_{22}Sn_5$) —and higher density.[1, 2]

In a conventional composite electrode design, the active materials and conductive additives (e.g., acetylene black) are bound together by a nonconductive polymer binder. The volume change of Sn-active materials tends to push away the acetylene black additive, leading to Sn particle isolation from the conductive network of the electrode laminate (**Figure 1a**). Thus, the capacity retention of a pure Sn composite electrode is very poor.[3, 4]

Numerous approaches have been proposed and developed to enable Sn-based electrode cycling with a reasonable reversible capacity. Some transition metals (e.g., Cu, Co) can form intermetallic compounds with Sn to provide an inactive matrix, which can deliver stable, long-term cycling performance.[5-14] Therefore, to alleviate the Sn volume change effect on cycling performance, a stress buffer phase was applied to fabricate Sn composite electrodes. The most-used material for stress relief is carbon, including amorphous carbon, graphite, graphene, and

nanotubes.[15-22] Building nanostructured Sn materials, such as nanowires, nanofibers, and nanotubes, is another approach to enable Sn cycling. The large surface area and special three-dimensional structure of nanomaterials alleviate the mechanical stress during Sn volume change, offer more void space to accommodate the volume change, and enhance the electronic connections.[23-27]

All the approaches mentioned above focus on the modification and preparation of Sn or Sn composite materials. However, at the particle level, higher degree of volume expansion of the Sn-based materials (compared to graphite) is still expected. The conventional electrode design is typically composed of active materials, a conductive additive, and a polymer binder. The polymer binder plays an important role in the cell's performance. Poly(vinylidene fluoride) (PVDF) and carboxymethylcellulose (CMC) are the conventional binders used for graphite anode, with only 10% of volume change of graphite material during the cycling. In a composite electrode with Sn as an active material, the Sn material is dispersed in a conductive matrix composed of a conductive additive (acetylene black) and a polymer binder. However the acetylene black does not have any flexibility to accommodate Sn expansion or extraction. Thus, after just a few cycles, the Sn materials disconnect from the acetylene black and lose the electrical connection with the current collector, leading to the capacity fade (**Figure 1a**).

It is critical to develop an improved approach to incorporate the Sn-based active materials into a composite electrode. The conductive polymer binder provides a unique advantage to assemble the alloy materials and to provide an electrical connection between the matrix and the alloy active materials.[28] Unlike the conventional approach, where the critical electrical conductivity

points are between the acetylene black particles and Sn particles, the conductive polymer binder-based Sn electrode has a closely bound electrical interface between the binder and Sn (**Figure 1b**).

The conductive binder Poly(9,9-dioctylfluorene-co-fluorenone-co-methylbenzoic ester) (PFM) used in this study is a polyfluorene-type polymer with two key function groups— carbonyl and methylbenzoic ester—for tailoring the polymer to be conductive in the Sn cycling potential range and for improving the mechanical binding force, respectively (**Figure 1c**). The conductive polymer binder is expected to bind closely to the lithium-storing Sn particles, even as they expand during lithiation and then shrink again during dislithiation. In the meantime, the electronic connection throughout the electrode is well maintained.

A new design principle for a conductive polymer binder for a lithium battery application was developed. Based on that principle, a PFM conductive polymer binder was developed and successfully used as both a binder and a conductive additive for a Si electrode.[28] Since Si and Sn work at a similar potential during lithiation and delithiation, the same polymer binder should be able to function for Sn-based materials. So far, only thin-film Sn electrodes (< 500 nm) have demonstrated acceptable capacity retention during lithiation and delithiation cycling tests in the literature. All pure Sn particle-based composite electrodes show very rapid capacity degradation during cycling. In this study, pure Sn nanoparticles were used to demonstrate the validity of the approach with a conductive polymer binder-based Sn composite electrode.

2. Experimental

The design, preparation, characterization and simulation of conductive polymer can be found in our published paper.[28] Sn nanoparticles were purchased from Sigma-Aldrich and used as received. The particle size defined by the company is < 150 nm. The purity is over 99% metal Sn content. The electrodes were made by dispersing a defined amount of Sn nanoparticle in the conductive polymer PFM chlorobenzene solution. The slurry mixing, electrode casting, and coin cell assembly can be found in the literature.[29] Three compositions of Sn electrode with PFM conductive polymer binder were fabricated at weight ratios of 98/2, 95/5 and 90/10 (Sn/PFM), and Sn mass loadings of 0.51 mg/cm^2, 0.22 mg/cm^2 and 0.32 mg/cm^2, respectively. Lithium-ion electrolytes were purchased from Novolyte Technologies, including 1 M $LiPF_6$ in ethylene carbonate (EC) and fluorinated ethylene carbonate (FEC) (EC:FEC at 3:7 w/w). Lithium metal was used as the counter electrode. The coin cell performance was evaluated with a Maccor Series 4000 Battery Test System in a thermal chamber at 30°C. The coin cells were cycled between 1.5V and 0.02V. A 200 kilovolt (kV) FEI monochromated F20 UT Tecnai was used to produce high-resolution TEM images of the Sn nanoparticles. The morphology of electrodes was imaged with a JEOL JSM-7500F field emission scanning electron microscope (SEM), and the electrode surface chemistry was mapped with an energy dispersive X-ray (EDX) analyzer from Thermo Scientific Analysis. The powder-specific surface areas were measured by a Brunauer-Emment-Teller (BET) N_2 adsorption method with a Micromeritics tristar surface area and porosity analyzer. The phase of powders was identified by a Philips X'Pert Pro Multipurpose X-ray Diffractometer using CuKα radiation (λ= 0.15406 nm). Adhesion measurements of the Sn electrode were performed on a Chatillon® TCD225 series force measurement system according to a previously reported method.[28]

3. Results and Discussion

3.1. Characterization of Sn Nanoparticles

Pure Sn nanoparticles were used as the active material in this study. The transmission electron microscopy (TEM) image in **Figure 2a** clearly shows their crystalline lattice morphology. The x-ray diffraction (XRD) of a Sn particle, as shown in **Figure 2b,** also confirms its crystalline structure. Measured *d* spacing from TEM image is 2.91$\mathring{A}$, which can be assigned to 2 2 0 (h k l) peak of Sn. The peaks of pristine Sn particles fully agree with reference (PDF # 04-0673) and can be indexed to a tetragonal Sn phase.

The secondary particles composed of primary particles (< 150 nm) were observed in SEM images (**Figure 2a**, inset). The surface area of the particle is 3.02 m^2 g^{-1} measured by the BET method. Assuming that the particles are spherical, equation (1) can be used to calculate their particle diamter (*d)*,

$d = 6 / (\rho \times a)$ (1)

where ρ is the density and *a* is the BET-measured surface area. In this case, *d* is 270 nm. As a primary Sn particle is < 150 nm, the larger diameter measured by BET must be for the secondary particle, which is consistent with scanning electron microscope (SEM) observations. Since BET measurement is based on gas absorption and de-absorption, it indicates that the primary particles are fused together to form secondary particles. Therefore, the primary Sn particles within the secondary particle are not accessible by the gas adsorption method. Likewise, the electrolyte is

not accessible in the internal secondary particles. The evaluation of cell performance has to be based on the secondary particles

In addition, for most metal nanoparticles, a native oxide layer can form on the surface of particles during the manufacturing process. It is known that an excessive native oxide layer degrades cell performance.[30, 31] Therefore, the surface morphology of Sn particles was carefully examined, and the surface was found to be free of the native oxide, based on TEM images. A thermalgravimetric analysis (TGA) further confirmed that the thickness of the native oxide layer was negligable.

3.2. Characterization of a Sn/Conductive Polymer Composite Anode

To characterize the electrochemical properties of Sn particles, electrodes based on Sn nanoparticles and a PFM conductive polymer binder were prepared. To optimize the electrode's composition, the ratios of Sn to conductive polymer binder were tuned from 98:2, 95:5 to 90:10 by weight. The electrode surface morphology was examined by SEM imaging, as shown in **Figure 3**. The morphology of electrodes with composition of 98:2 and 95:5 rations of Sn to Condcutive polymer binder (**Figure 3a** and **3b**) is similar, exhibiting the features of tightly bound Sn nanoparticles with pores. The polymer binder is distributed evenly on the surface of the Sn nanoparticles, therefore the polymer binder cannot be identified as a separate phase, based on SEM images of **Figure 3a** and **3b**.[32]

The presence of a polymer on the surface of the Sn in the electrode can be detected by an energy dispersive X-ray (EDX) mapping technique. Since the electrodes only have two components, Sn

and PFM polymer, carbon from the polymer was taken as the element to map the distribution of the polymer in the electrode. The carbon elemental mapping (**Figure 3a** and **3b**, insets) of the electrodes (98:2 and 95:5 compositions) showed that the conductive polymer binder was uniformly distributed in the electrodes. When the conductive polymer content increases to 10% by weight (**Figure 3c**), an obvious aggregation of Sn particles and a thick layer of polymer coating on the surface of electrode can be clearly observed by SEM imaging. The carbon elemental mapping of this electrode (**Figure 3c**, inset) shows higher intensity than those of the other two electrodes. This confirms an increase of polymer content in the electrode. Due to the higher density of the Sn than that of the polymer binder, the 10% of weight content of binder makes up close to 50% volume fraction in the electrode. Therefore, a dramatic decrease of pores in the electrode with 10% weight binder was observed due to the high polymer content (**Figure 3c**). The calculated porosity for 2% and 5% binder electrodes is 75.6% and 79.8%, respectively; however, the porosity decreased dramatically to 43.1% for the electrode containing 10% binder. All the calculated values are consistent with the observations based on SEM images.

Assuming that the polymer coats the surface of the secondary Sn particles, the volume of polymer (V) in the electrode can be calculated based on equation (2), where m is the mass of polymer in the electrode, andρ is the polymer density.

$$V = m / \rho \qquad (2)$$

For Sn particles, the total surface area (A) can be calculated from equation (3), where, a is the BET surface area of Sn particles in $m^2 g^{-1}$ and m is the total mass of Sn in the electrode.

$$A = a \times m \qquad (3)$$

Thus, the thickness of polymer (d) coated on Sn particles in the electrode can be estimated from equation (4).

$$d = V / A \qquad (4)$$

The thickness of the polymer coating in electrodes containing 2% and 5% binder was calculated to be 3.98 nm and 9.43 nm, respectively. For a 10% binder electrode, the polymer coating increased to 21.6 nm thick. At a low loading of Sn filler, the polymers tend to fill in the porosity created by the Sn particles, creating polymer- and particle-rich domains that are observable in an SEM image (**Figure 3c**).

3.3. Electrochemical Performance of Sn and the Conductive Polymer Composite Anode

To test the electrode performance, the coin cells with lithium metal as the counter electrode were assembled and tested at 0.1C current density in the potential range from 20 millivolt (mV) to 2 volts (V). In this potential range, the Sn can be fully lithiated and delithiated. The expected volume change is about 300% during this process.

Figure 4 and **Supplimental Figure 1** show the cycling performance of the electrodes of different binder content. The three different compositions of electrodes show their different cycling behaviors. For an electrode with a 2% binder, the initial delithiation capacity can reach 740 mAh/g and then drop quickly in its first 20 cycles to below 300 mAh/g. This quick fading is most likely because a 2% binder is not enough to adhere the Sn electrode materials together. Also, delamination of the electrode from the Cu current collector was observed after only a few cycles. The low binding force caused the Sn to break away from the electric connections, which led to a quick capacity fade.

However, cycling performance was significantly improved as the binder content was increased to 5%. The capacity was 620 mAh/g in the initial cycles, and then it gradually stabilized at 510 mAh g^{-1} after 40 cycles. The polymer binder at 5% content seems enough to provide a good mechanical adhesion for the electrode. To confirm that, the force needed to peel the electrode materials from the current collector was measured. It was found that 1.8 pound force (lbf) of force was needed to peel the laminate with 2% binder off from the current collector. Under the same condition, to peel off the laminate containing 5% binder, the force had to be increased to 4.5 lbf, which is more than double the adhesion force of the electrode containing the 2% binder. The adhesion strength is very important for the Sn electrodes made of conductive polymer binder. Better adhesion between Sn and the binder assures the physical integration of the electrode. Moreover, the electric conductivity is governed by the interface of Sn and the conductive binder. Tight association of the Sn with the binder affords better and lasting electric conduction in the electrode. This is critical for stable cycling of alloy materials.

Although higher binder content can lead to improved adhesion, the use of excessive polymer binder must be avoided because too much polymer could slow the diffusion of lithium-ions in the electrode and at the interface and decrease active material loading. The adverse effects of the binder were observed in the electrode containing 10% binder. As previously calculated, the polymer layer on Sn particles in a 10% binder electrode is about 21.6 nm. In this case, the polymer in the electrode with 10% binder needs a longer period of time to be activated before the Sn particles are fully cycled, and the diffusion of lithium-ion through this thick polymer layer is much slower than other two electrodes. Thus, the initial discharge capacity is extremely low for

the 10% binder electrode. It took about 40 cycles to slowly reach 510 mAh/g of reversible capacity.

Electrode porosity also plays a key role in cycling performance. In electrodes with both 2% and 5% binder, the porosity is above 70%. The high porosity is critical for the performance of large volume change alloy materials, as volume expansion tends to reduce porosity and slow the electrode's lithium-ion diffusion rate. The electrode with a 10% binder has 43.1% porosity. Without proper porosity, the lithium-ion transport in the electrode is hindered, especially after Sn volume expansion. The formation of thick solid electrolyte interphase (SEI) layer on the surface of Sn particles further reduces the porosity.

To verify the morphology change of the electrode after cycling, the cells based on different electrodes were disassembled after one cycle. The cycled electrodes were examined by SEM, as shown in **Figure 5**. Compared with fresh electrodes (**Figure 3**), both pore size and number were reduced due to the volume expansion of Sn particles and the SEI layer formed on the surface of the particles. For electrodes containing 2% and 5% binder, pores still can be observed; however, for electrodes containing 10% binder, the pores were completely sealed off. Sn particles are fully covered by a thick layer of polymeric materials. In this case, the lithium-ion has to diffuse through the thick layer of coating to reach the Sn particles, due to deficient porosity.

As shown in **Figure 4**, the electrode containing the 5% binder shows the best cycling performance, so the electrode with this composition was selected for rate performance tests. To characterize the rate capability of Sn nanoparticles, three different rate tests were conducted:

symmetric charge (lithiation) and discharge (delithiation) rates; 0.1C discharge and various charge rates; and 0.1C charge and various discharge rates. **Figure 6** shows the rate performance of the electrode under different testing conditions. The cell shows the best performance at 0.1C charge and various discharge rates. With 0.1C charge current density, the cell can cycle at a 20C discharge rate with 235 mAh/g reversible capacity. At a 2C discharge rate, the reversible capacity is 380 mAh/g, which is comparable with the theoretical capacity of graphite (372 mAh/g). The cells show different performance with 0.1C constant discharge and various charge rates. Before a 1C testing rate, the performance trend is very close to that of a 0.1C charge and various discharge tests. However, after the charge rate increased to 2C, the reversible capacity decayed to 150 mAh/g. This variation shows that the control factor of rate performance of Sn materials is a charge process, not a discharge process. If Sn nanoparticles are given enough time to alloy with lithium, they can release the lithium at a relatively high current rate. This was further confirmed by the symmetric charge and discharge rate test, which shows the worst performance in these three tests. After rate tests, the cells can recover their initial capacity, which means that the structure of Sn nanoparticles is not destroyed during the process where they alloy and de-alloy with lithium, even at high rates.

3.4. Sn Nanoparticle Phase Change After Long-term Cycling

Although the phase change during charge and discharge of a pure nano Si particle has been extensively studied, the pure Sn nanoparticle structure change after cycling has not been reported. In particular, the Sn phase change after long cycling has not been studied because of the inability to acquire an extended-cycled pure Sn sample.

To monitor the phase change of Sn particles, the cells were disassembled after 10 cycles and 150 cycles. To identify the phase change of Sn particles after cycling, the XRD diffraction pattern of Sn particles, fresh electrode, and cycled electrode (10 and 150 cycles) were collected and compared, as shown in **Figure 7**. Since the laminate is coated on a Cu current collector and X-ray can penetrate the laminate to pick up the Cu peak in XRD spectra, the Cu reference spectra (PDF # 04-0836) is provided for an easy comparison. The XRD spectra of a fresh Sn electrode show the clear Sn peaks. The extra peaks at 41^{o} and 48^{o} of fresh electrode can be attributed to a polymer, which is present in XRD spectra of cycled Sn electrodes too. After 10 cycles, the Sn peaks still can be observed; however, the intensity is decreased compared with the pristine electrode, indicating that the crystalline structure of Sn particles starts to fade. After long-term cycling (150 cycles), the Sn peaks cannot be observed in the XRD graph. Based on these observations, the crystalline Sn gradually degrades to amorphous during the cycling.

The phase change also can be observed from its potential profiles (**Figure 7b**). In the initial two cycles, the typical plateaus correspond to the lithiation or delithiation of lithium at two phase regions of the alloy. The plateaus became a slope after 150 cycles, indicating the amorphization of the structure.

The TEM technique was used to observe both the crystallinity change and particle-level morphology changes. The cells after different cycles (4 and 190 cycles) were dissembled, and the cycled electrodes were examined by TEM. **Figure 8a** shows the pristine spherical Sn particles. The crystalline features of the Sn particle can be clearly identified in the high-magnification TEM image in **Figure 8d**. After 4 cycles, some of the spherical Sn particles turned into irregular

shapes (**Figure 8b**). However, the crystalline domains of particles still can be observed with a high-resolution TEM image (**Figure 8e**). In addition, after 4 cycles, Sn particles are strongly embedded in the polymer matrix, as the arrow indicates in **Figure 8b**.

The morphology of Sn particles totally changed after 190 cycles. The primary Sn particles tend to pulverize and re-aggregate after repeated volume expansion and extraction (**Figure 8c**). The Sn particle pulverizes to small fractions but remains embedded in the conductive polymer network, maintaining the integrity of the electrode (**Figure 8f**). After long-term cycling, Sn lost all the crystalline features and thoroughly turned amorphous. Most of the capacity fading after cycling is due to the pulverization of the Sn nanoparticles; the conductive polymer to Sn adhesion is still largely maintained.

3.5. Comparison of Different Binders for Sn Nanoparticle Composite Anode

Sn is a highly conductive metal. Therefore, the need for a conductive additive in the electrode is not obvious. Non-conductive binder such as PVDF and CMC may work with Sn based electrode. To investigate the electrode performance of Sn nanoparticle with different binders , conventional binders as PVDF and CMC were fabricated into electrode with Sn nanoparticles, and tested. The performances of these electrodes were compared with that of the electrode fabricated with the conductive polymer binder (PFM). The electrode composition for CMC and PFM binders is 5% binder and 95% Sn. Due to the insulating nature of PVDF, its content in the electrode had to be decreased to 2%.

All the cells were tested under the same conditions. **Figure 9a** shows the cell cycling performance based on the different binders. For the CMC binder, the discharge capacity fades dramatically from initial 740 mAh/g in 20 cycles. Cell performance is even worse with the PVDF binder. With only 2% of PVDF used in the electrode, almost no discharge capacity can be achieved, due to the insulating effect of the PVDF. In both the PVDF and CMC cases, the Sn electrode is electrically connected at the initial stage, due to the Sn particle aggregation. However, after only a few charge and discharge cycles, the Sn particles are no longer in contact with each other. The insulating binders do not provide electrical connections to the Sn particles.

For comparison, the cell with 5% of conductive binder shows over 500 mAh/g reversible discharge capacity because of its conductive and binding properties. An important factor to evaluating binder properties is binding capability, which can assure electrode integrity during cycling. It is known that CMC has a stronger binding force to the current collector than does PVDF because its carboxylic groups can form the hydrogen binding with Sn particles. Using the same principle, our conductive polymer binder has ester groups that also can provide strong binding between the laminate and the current collector.

To quantitatively evaluate the binding force of the three binders, peeling tests were conducted. The test results are shown in **Figure 9b**. The laminate with 2% of PVDF binder is most easily peeled off from the current collector. Conversely, CMC adhesion is much stronger than that of the PVDF. The electrode containing PFM is extremely robust. The binding force of PFM is much greater than either PVDF or CMC, and it can maintain electrode integrity during cycling. This is

another reason that an electrode based on the conductive polymer binder exhibits the best performance.

4. Conclusions

The conductive polymer binder provides a new method to connect large-volume changing alloy anode materials. This new approach demonstrated the first time that pure Sn nanoparticle-based composite electrodes can be extensively cycled at high capacity. The results further support the validity of the conductivity and adhesion bi-functional design of the binders. Compared with conventional PVDF and CMC binders, the conductive polymer binder can significantly improve the cycling performance at 520 mAh/g reversible capacity. Since the conductive polymer binder constitutes only 5% of the electrode, the active material content (95%) in the electrode is much higher than the normal Sn composite electrode, which has an additional conductive additive component. The reversible capacity of the electrode containing 5% conductive polymer binder can reach close to 500 mAh/g, even when accounting for the total electrode material mass. In addition, pure Sn nanoparticles gradually lose their crystallites and pulverize after repeated alloying and de-alloying with lithium. In the case of the conductive polymer, it has the advantage of providing the conductive matrix to embed the particles and even their fractions after cycling. Thus, the conductive polymer is an efficient strategy to enable the cycling of a metal-based electrode with volume change problems.

Acknowledgements

This work was funded by the Assistant Secretary for Energy Efficiency, Office of Vehicle Technologies of the U.S. Department of Energy (U.S. DOE) under contract no. DE-AC02-

05CH11231 under the Batteries for Advanced Transportation Technologies (BATT) Program, and by the University of California, Office of the President through the University of California Discovery Grant. TEM was performed at National Center for Electron Microscopy, funded by Office of Science, Office of Basic Energy Sciences, of the U.S. DOE under Contract No. DE-AC02-05CH11231.

References

1. M. Winter and J. O. Besenhard, Electrochim. Acta **45** (1-2), 31-50 (1999).
2. A. R. Kamali and D. J. Fray, Rev. Adv. Mater. Sci. **27** (1), 14-24 (2011).
3. P. Lavela, F. Nacimiento, G. F. Ortiz and J. L. Tirado, J. Solid State Electrochem. **14** (1), 139-148 (2010).
4. T. Zhang, L. J. Fu, J. Gao, Y. P. Wu, R. Holze and H. Q. Wu, J. Power Sources **174** (2), 770-773 (2007).
5. X. M. Zheng, L. Huang, Y. Xiao, H. Su, G. L. Xu, F. Fu, J. T. Li and S. G. Sun, Chem. Commun. **48** (54), 6854-6856 (2012).
6. J. Z. Chen, L. Yang, S. H. Fang and S. Hirano, J. Power Sources **209**, 204-208 (2012).
7. S. Yoon and A. Manthiram, Electrochim. Acta **56** (8), 3029-3035 (2011).
8. X. L. Wang, M. Feygenson, H. Y. Chen, C. H. Lin, W. Ku, J. M. Bai, M. C. Aronson, T. A. Tyson and W. Q. Han, J. Am. Chem. Soc. **133** (29), 11213-11219 (2011).
9. M. V. Reddy, G. V. S. Rao and B. V. R. Chowdari, J. Mater. Chem. **21** (27), 10003-10011 (2011).
10. I. Issac, M. Scheuermann, S. M. Becker, E. G. Bardaji, C. Adelhelm, D. Wang, C. Kubel and S. Indris, J. Power Sources **196** (22), 9689-9695 (2011).
11. F. Huang, X. Z. Lu, Y. Liu, J. Liu and R. Wu, Mater. Sci. Technol. **27** (1), 29-34 (2011).
12. X. L. Wang, W. Q. Han, J. J. Chen and J. Graetz, ACS Appl. Mater. Inter. **2** (5), 1548-1551 (2010).
13. M. D. Fleischauer, M. N. Obrovac and J. R. Dahn, J. Electrochem. Soc. **155** (11), A851-A854 (2008).
14. L. B. Wang, S. Kitamura, T. Sonoda, K. Obata, S. Tanase and T. Sakai, J. Electrochem. Soc. **150** (10), A1346-A1350 (2003).
15. Z. H. Wen, S. M. Cui, H. J. Kim, S. Mao, K. H. Yu, G. H. Lu, H. H. Pu, O. Mao and J. H. Chen, J. Mater. Chem. **22** (8), 3300-3306 (2012).
16. G. Wang, Y. Q. Ma, Z. Y. Liu and J. N. Wu, Electrochim. Acta **65**, 275-279 (2012).

17. B. Luo, B. Wang, X. L. Li, Y. Y. Jia, M. H. Liang and L. J. Zhi, Adv. Mater. **24** (26), 3538-3543 (2012).

18. X. F. Li, A. Dhanabalan, L. Gu and C. L. Wang, Adv. Energy Mater. **2** (2), 238-244 (2012).

19. Y. Yu, L. Gu, C. B. Zhu, P. A. van Aken and J. Maier, J. Am. Chem. Soc. **131** (44), 15984-15985 (2009).

20. Y. Wang, M. Wu, Z. Jiao and J. Y. Lee, Chem. Mater. **21** (14), 3210-3215 (2009).

21. Y. S. Jung, K. T. Lee, J. H. Ryu, D. Im and S. M. Oh, J. Electrochem. Soc. **152** (7), A1452-A1457 (2005).

22. B. Veeraraghavan, A. Durairajan, B. Haran, B. Popov and R. Guidotti, J. Electrochem. Soc. **149** (6), A675-A681 (2002).

23. M. Tian, W. Wang, Y. J. Wei and R. G. Yang, J. Power Sources **211**, 46-51 (2012).

24. G. Ferrara, C. Arbizzani, L. Damen, M. Guidotti, M. Lazzari, F. G. Vergottini, R. Inguanta, S. Piazza, C. Sunseri and M. Mastragostino, J. Power Sources **211**, 103-107 (2012).

25. J. Z. Wang, N. Du, H. Zhang, J. X. Yu and D. R. Yang, J. Phys. Chem. C **115** (47), 23620-23624 (2011).

26. H. R. Jung and W. J. Lee, J. Electrochem. Soc. **158** (6), A644-A652 (2011).

27. N. S. Choi, Y. Yao, Y. Cui and J. Cho, J. Mater. Chem. **21** (27), 9825-9840 (2011).

28. G. Liu, S. Xun, N. Vukmirovic, X. Song, P. Olalde-Velasco, H. Zheng, V. S. Battaglia, L. Wang and W. Yang, Adv. Mater. **23** (40), 4679-4683 (2011).

29. G. Liu, H. Zheng, A. S. Simens, A. M. Minor, X. Song and V. S. Battaglia, J. Electrochem. Soc. **154** (12), A1129-A1134 (2007).

30. S. Xun, X. Song, M. E. Grass, D. K. Roseguo, Z. Liu, V. S. Battaglia and G. Liu, Electrochem. Solid-State Lett. **14** (5), A61-A63 (2011).

31. S. Xun, X. Song, L. Wang, M. E. Grass, Z. Liu, V. S. Battaglia and G. Liu, J. Electrochem. Soc. **158** (12), A1260-A1266 (2011).

32. G. Liu, H. Zheng, X. Song and V. S. Battaglia, J. Electrochem. Soc. **159** (3), A214-A221 (2012).

Figures

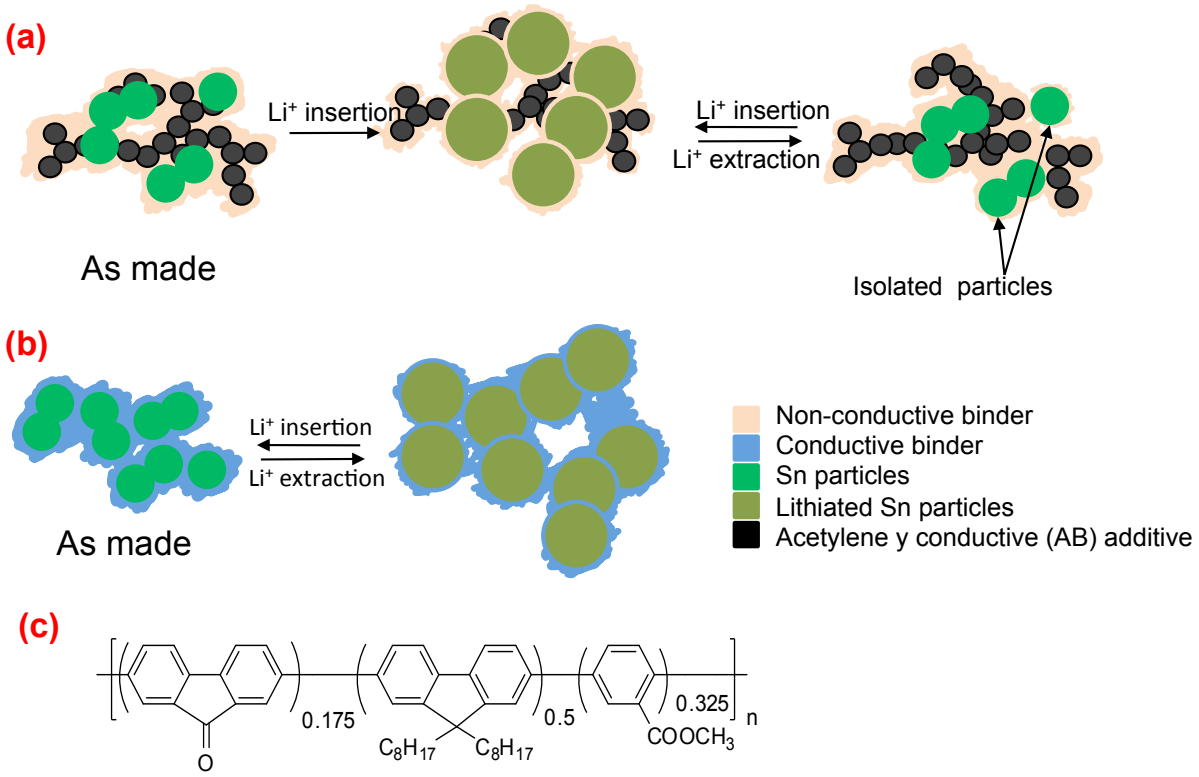

Figure 1. (a) Sn in a traditional composite electrode with an acetylene black conductive additive and a non-conductive polymer binder. (b) Sn in the conductive polymer binder electrode. (c) Conductive polymer binder PFM molecular structure.

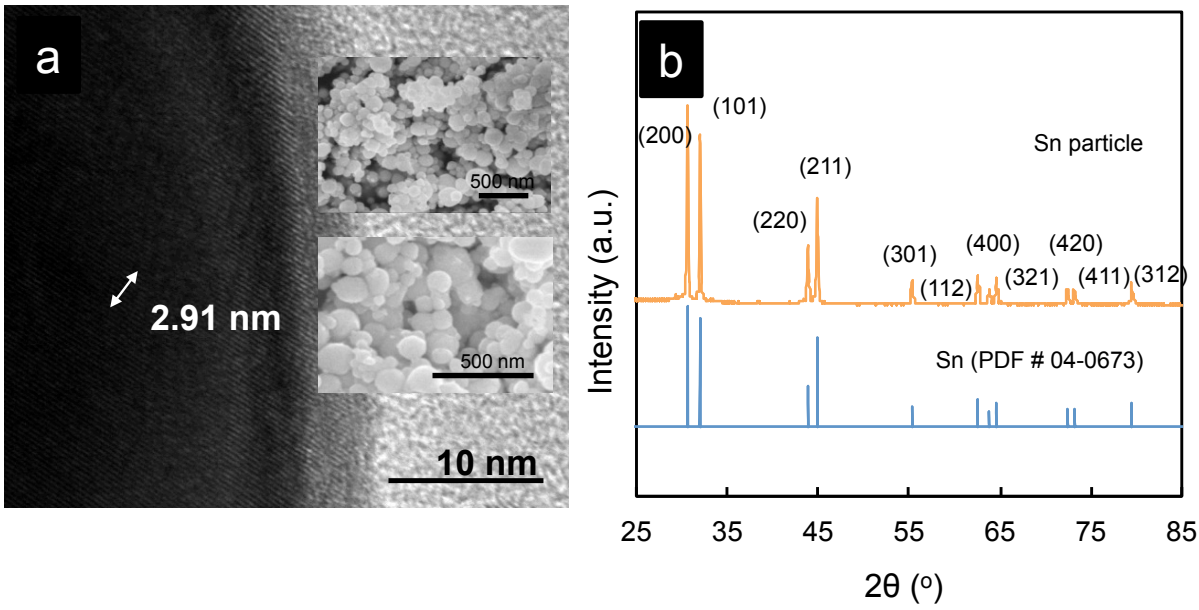

Figure 2. (a) TEM and SEM (insets) images of nano Sn particle. (b) XRD of Sn particles.

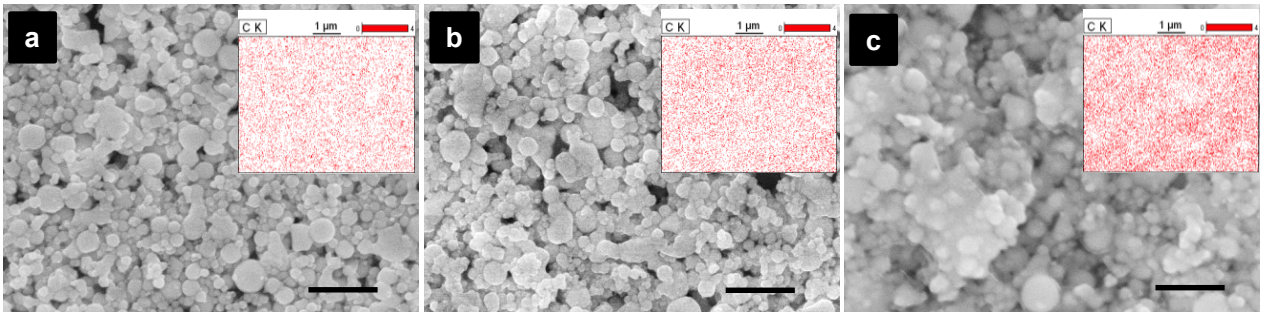

Figure 3. SEM images of an electrode with different binder contents (a) 2%; (b) 5%; (c) 10%.

Scale bars: 1µm; insets: EDX mapping of carbon.

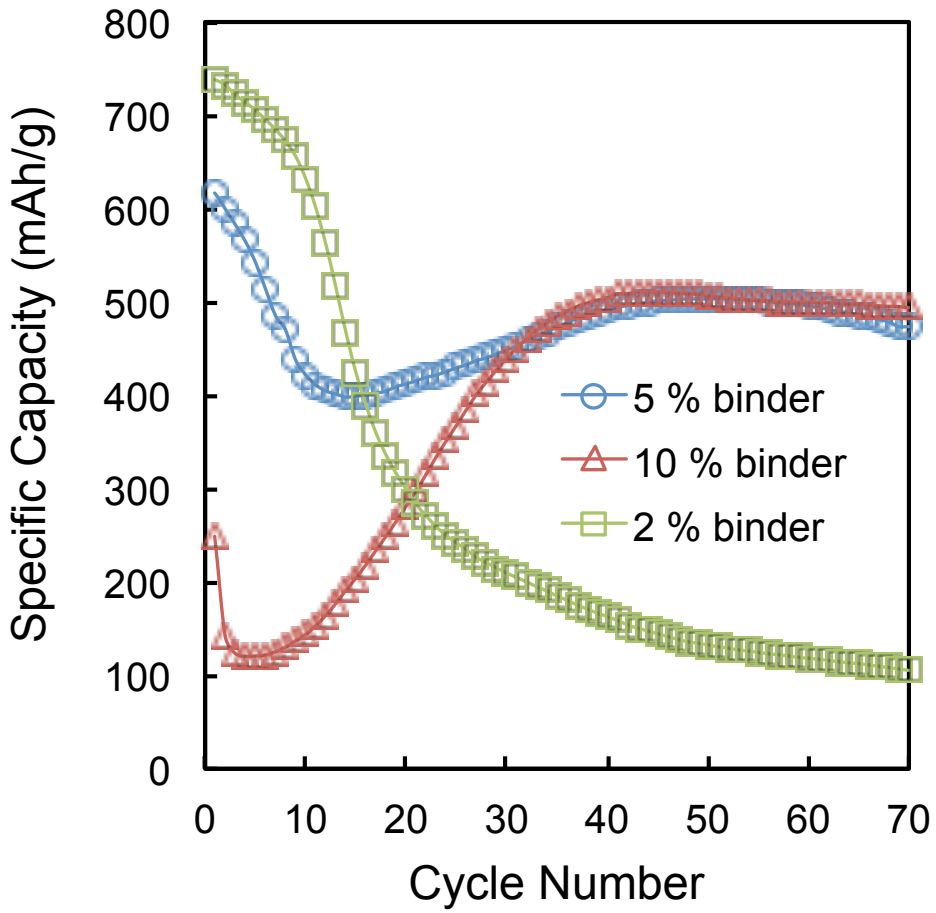

Figure 4. Discharge (delithiation) capacity of Sn electrodes with different binder contents at 0.1C rate between 1.5V and 20 mV.

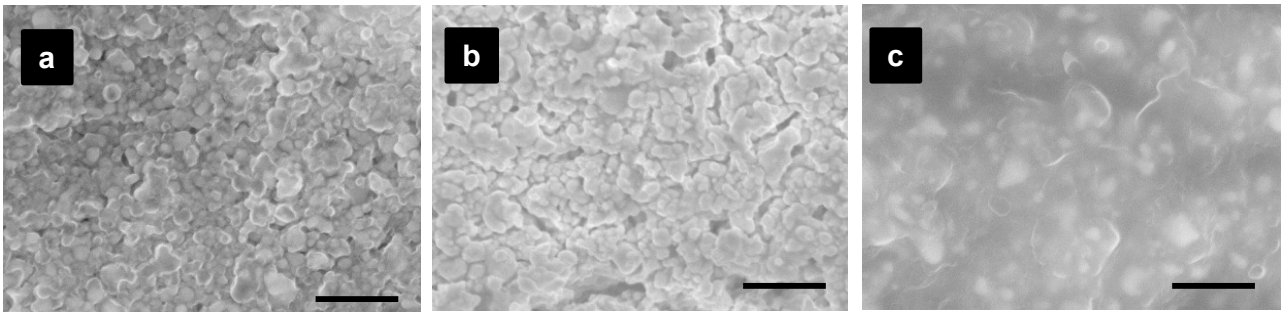

Figure 5. SEM images of the electrodes of different composition after 1 cycle: (a) 2% binder; (b) 5% bidner; (c) 10% binder. Scale bar: 1 μm.

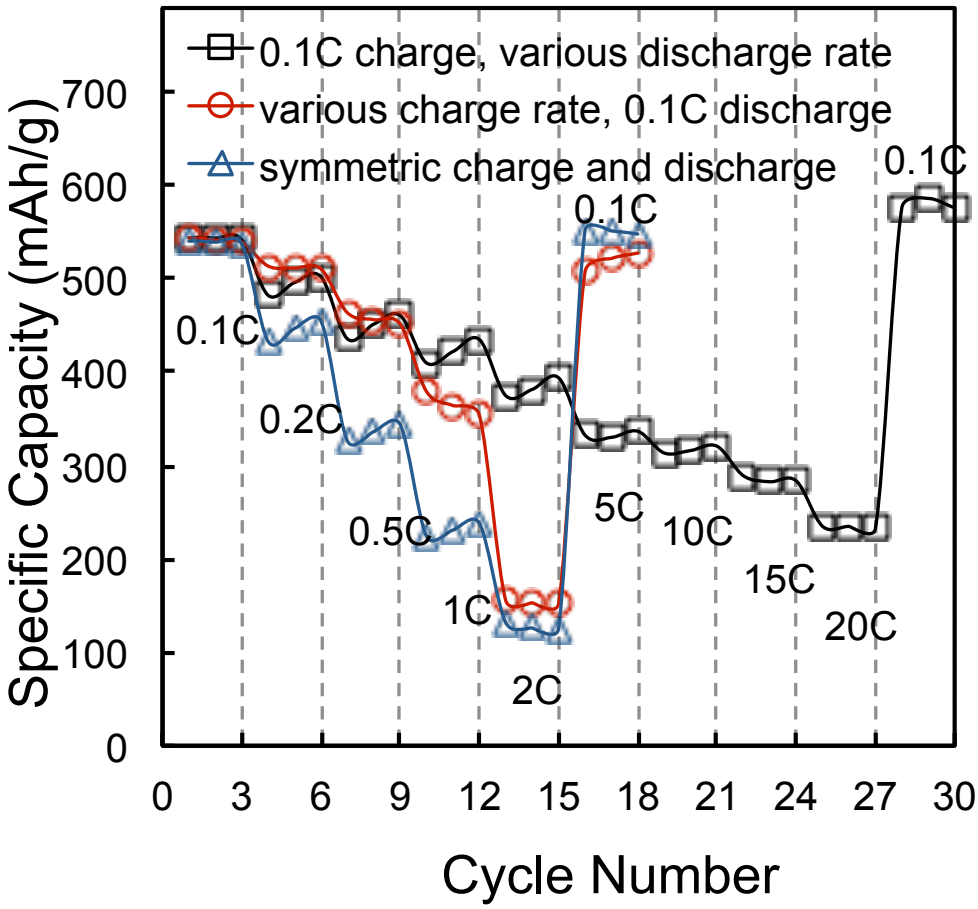

Figure 6. Discharge rate performance of the Sn/PFM (95/5) composite electrode.

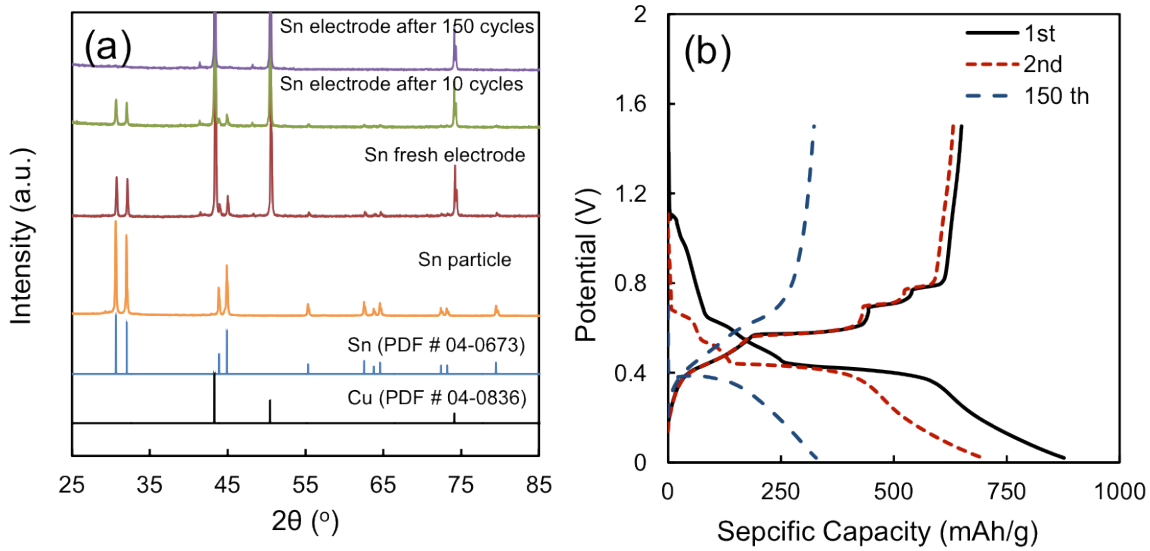

Figure 7. (a) XRD of Sn particles and a Sn electrode before and after cycling (Sn/PFM 95/5). (b) Sn electrode potential profiles.

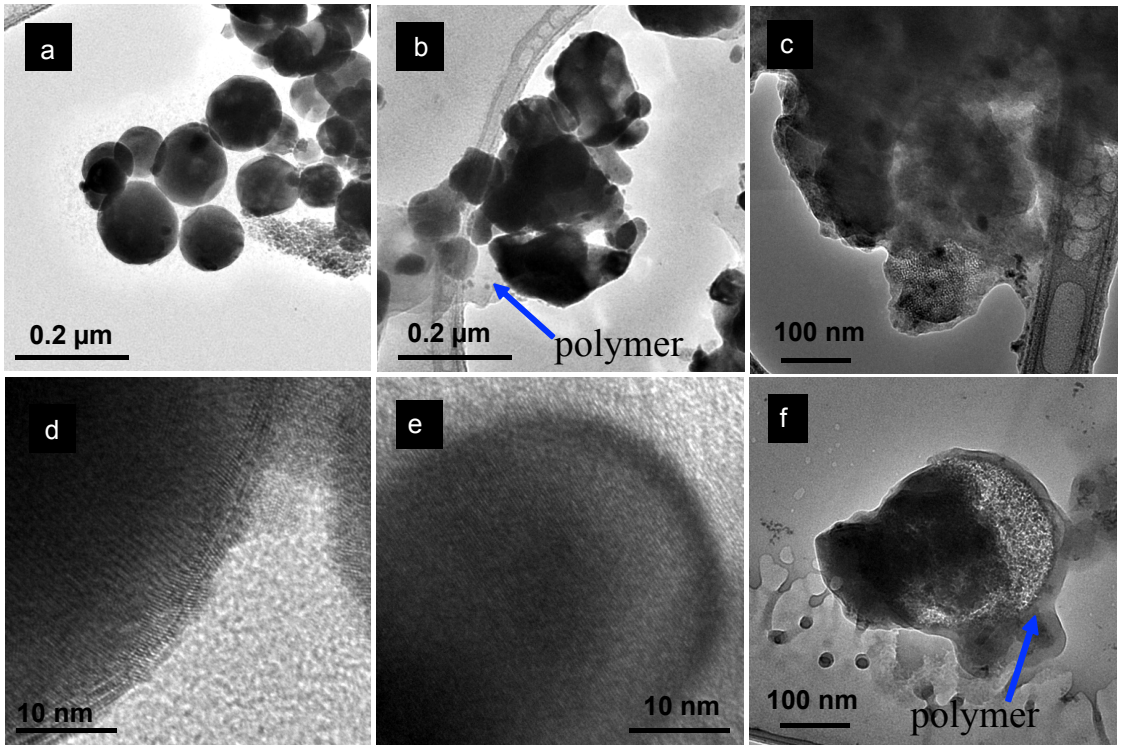

Figure 8. TEM images of Sn particles: (a, b) pristine; (b, e) after 4 cycles; (c, f) after 190 cycles.

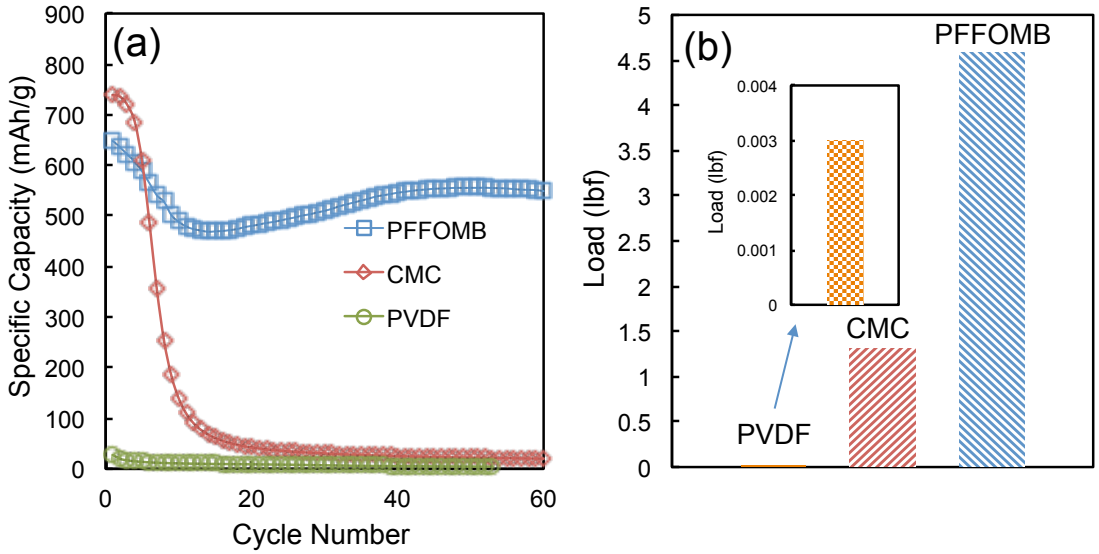

Figure 9. (a) Comparison of discharge capacity of Sn materials with different binders: PFM (5%), CMC (5%) and PVDF (2%). (b) The adhesion force test data is based on different binders.